Unveiling the Potential of P3 Phase in Enhancing the Electrochemical Performance of a Layered Oxide Cathode

Hari Narayanan Vasavan ^a, Manish Badole ^a, Samriddhi Saxena ^a, Velaga Srihari^b, Asish Kumar Das ^a, Pratiksha Gami ^a, Sonia Deswal ^c, Pradeep Kumar ^c, and Sunil Kumar ^{a,*}

^a Department of Metallurgical Engineering and Materials Science, Indian Institute of Technology Indore, Simrol, 453552, India.

^b High Pressure & Synchrotron Radiation Physics Division, Bhabha Atomic Research Centre, 400085 Mumbai, India

^c School of Physical Sciences, Indian Institute of Technology Mandi, Himachal Pradesh, 175005, India

^{*} Corresponding Author, sunil@iiti.ac.in

Abstract

Controlling the phase structure of layered oxide cathodes is considered an effective strategy to realise high-performance Na-ion batteries. Herein, we unveil the synthesis and electrochemical behaviour of hitherto unreported monophasic P3 structure in Na_{0.75}Mn_{0.75}Ni_{0.25}O₂ (NNM) calcined at 750 °C. The conversion of P3 to P2-type single phase (at 850 °C) upon increasing the calcination temperature, with P2/P3 biphasic structures at intermediate temperatures, was confirmed by the Rietveld refinement of the x-ray diffraction (XRD) data. The monophasic P3 cathode showed a specific capacity of 190 mAh/g at 0.1C and retained 90% of its initial capacity after 200 cycles at 1C in the 1.5-4.2 V range. The GCD curves also showed a decrease in specific capacity with an increase in the P2 phase. The P3-dominant biphasic cathodes displayed superior rate performance exhibiting capacities up to 97 mAh/g at 6C, attributed to its smaller particle size and an optimal P2/P3 phase fraction. *Operando* Synchrotron XRD data confirmed the suppression of P3→O'3+O3 transformation in biphasic cathode that was present in monophasic P3 structure during charge-discharge cycling. The superior electrochemical performance and excellent structural stability of biphasic cathode make it ideal for stationary and mobile storage applications.

KEYWORDS: Layered oxides; Biphasic cathode; *Operando* Synchrotron XRD; Electrochemical behavior; Rate performance

1. Introduction

Na-ion batteries (NIBs) are an important development in energy storage, offering a costeffective, safe, and environmentally friendly alternative to lithium-ion batteries (LIBs) [1-5]. Along with the considerably higher abundance of sodium, NIBs share the same working principle (rocking-chair mechanism) and have similar components as LIBs allowing their seamless integration into the current battery manufacturing eco-systems [6-11]. Among the different battery components, cathodes are the most crucial in determining a cell's overall cost and performance. Research studies on identifying cathode materials in Na-ion batteries mainly concentrate on layered oxides (LOs), NASICON, and Prussian blue analogs type materials [11-13]. Among these, cathodes based on LOs, primarily due to their compositional diversity, higher specific capacity, and easier synthesis, show the most promise[14-16]. Generally, layered oxides (with the general formula Na_xTMO2) are subclassified into P2, P3, and O3 based on their thermodynamic stability. In P2 and P3-type materials, the Na-ion occupies a prismatic site as opposed to an octahedral site in the O3-type compounds. Further, in a P2-type framework, Na-ions occupy 2 different prismatic sites, which are either facesharing (Na_f) or edge-sharing (Na_e) with the transition metal octahedron (TM-O₆). In P3, all prismatic sites are crystallographically equivalent Na_f sites [17].

The literature on various structures and electrochemical properties of P2 and O3-type cathode materials is quite extensive [4, 18-20]. Materials based on a P2-type framework possess notable features such as improved electrical conductivity and cyclic stability compared to the other structures because of their relatively open structure and resilience to resist phase transformations during the extraction of Na-ions [21-23]. O3-type materials typically exhibit higher specific capacities but suffer from poor rate performance and cyclic stability. In contrast, research on thermodynamically stable P3-type materials has only recently started to emerge [20, 24-27]. The studies on the P3 phase primarily revolve around those obtained

electrochemically during the charging of O3-type cathodes, where the diffusion coefficient of the material shows a sharp rise [24, 28]. New reports on thermodynamically synthesized P3-type materials also suggest high diffusion coefficients comparable to that of P2-type materials [27, 29, 30]. However, rapid structural changes during cycling render this ineffective as other phases (O3, O'3, and P'3 that form at lower and higher voltages) do not support fast Na-ion kinetics, severely limiting the rate performance of these P3 phases [30-32].

Among various cathode materials investigated for NIBs, compounds based on the Na_yMn_{0.65+x}Ni_{0.35-x}O₂ (NNMO) system (with both P and O-type frameworks) have a huge potential for commercial applications. Compounds in this system typically use Ni^{2+/4+} redox reactions to achieve maximum specific capacity, while Mn-ions stabilize the structure during Na⁺ extraction [19, 31, 33, 34]. Several studies on this system have identified P2-type Na_{0.67}Mn_{0.67}Ni_{0.33}O₂ as the optimized cathode that maximizes the Ni²⁺ concentration while eliminating Jahn-Teller active Mn³⁺ ions from the structure. The cathode reportedly delivers a specific capacity of 130 mAh g⁻¹ between 2-4.2V, with more than 70% capacity retention after 100 cycles. While operating in the broader voltage window between 1.5-4.2 V, the cathode can deliver capacities close to 160 mAh g⁻¹ due to the activation of Mn^{3+/4+} redox couple but suffers increased capacity degradation after each cycle [3, 21, 35-37].

Several methods, such as surface modification and substitution of Mn/Ni with other active/inactive elements, have made significant headways in improving the cyclic stability of the compound but with a drastic reduction in the specific capacity. In contrast, techniques involving hybrid cathodes of P2/O3 have shown similar enhancements in cyclic stability without compromising specific capacity [14, 15, 38, 39]. Further, biphasic cathode materials involving P2/O3 have also shown relatively better success in mitigating the structural distortion caused by the activation of Mn^{3+/4+} in NNMO. This allows a wider operational voltage window during cycling, substantially boosting the specific capacity [15, 40].

Herein, we designed a series of P3/P2 biphasic Na_{0.75}Mn_{0.75}Ni_{0.25}O₂ (NNM) cathode with varying P2/P3 phase fractions and report on the impact of a varying P3 phase on the electrochemical properties in a wider optional window between 1.5-4.2 V. NNM (with a lower concentration of Ni) was chosen over NNMO, as the titled cathode material, to increase the redox activity of Mn³⁺ during cycling. This allowed a better investigation of the role of P3 concentration in the overall resilience of the biphasic cathode towards severe structural distortions. The variable concentration of the P3 phase, ranging from 0-100%, was achieved by appropriately tuning the calcination temperature. The P3 phase typically forms a lower temperature compared to P2 and O3 phases. This was found to have profound implications on the morphology and electrochemical properties of the cathode material, with P3 dominant biphasic cathodes showing substantially superior rate performance and cyclic stability compared to monophasic P2 and P3 cathodes. Apart from morphological changes, the manifestation of the synergetic effect between the two phases mitigated the effects of severe structural distortions induced during cycling, resulting in a better cyclability of the biphasic cathodes.

2. Experimental

2.1. Synthesis

A conventional sol-gel method was used to prepare the P2/P3-Na_{0.75}Mn_{0.75}Ni_{0.25}O₂ series of cathode materials. A homogeneous solution containing stoichiometric amounts of manganese (II) acetate tetrahydrate, nickel acetate tetrahydrate, and sodium carbonate was prepared in DI water and stirred for 6 h after which ethylene glycol and citric acid were added. After stirring for another 12 h, the solution was heated to produce a gel. The gel was then dried and subsequently ground to obtain a powder. The powder was heat treated at 550 °C in air for 12 h and calcination at different temperatures (700 – 850 °C) to obtain the final product.

2.2. Structural Characterization

The powder x-ray diffraction (XRD) patterns were obtained at room temperature using Malvern Pan Analytica's, Empyrean, diffractometer (Cu-Kα radiation source) between 10°-80° 20 range. The crystallographic data for the samples were obtained through Rietveld refinement of the XRD data with the help of TOPAS Academic (version 6) software package [41]. The microstructure was analyzed using a Joel field emission scanning electron microscope (model JEOL-7610) equipped with energy-dispersive x-ray spectroscopy (EDS) for elemental mapping. X-ray photoelectron spectra (XPS) were obtained using a Thermofisher Scientific -Naxsa base with an Al Ka X-ray source (1486.6 eV). The Mn and Ni K-edge extended x-ray absorption fine structure (EXAFS) spectra were obtained from the scanning EXAFS beamline (BL-9) at Indus-2 synchrotron source (2.5 GeV, 150 mA) at Raja Ramanna Centre for Advanced Technology (RRCAT) Indore, India, and were analyzed using ATHENA and ARTEMIS software packages [42]. Operando Synchrotron XRD studies were carried out using extreme conditions angle dispersive/energy dispersive synchrotron X-ray diffraction (BL11) at Indus-2 beamline (RRCAT) with a beam wavelength of 0.8312 Å and beam energy of 2.5 GeV in transmission mode. The CR2032 coin cells for the operando studies were prepared by drilling 3 mm holes in the cathode and anode casings which were sealed using Kapton films.

2.3. Electrochemical Characterization

The positive electrode slurry was prepared by mixing the active material, Ketjen black, and PVDF binder in NMP in a wt. ratio of 75:10:15. The slurry was cast onto an Al current collector, dried, and punched into 16 mm discs. CR2032 coin cells were fabricated for electrochemical tests of cathodes using the Na metal as the counter electrode, 1M NaClO₄ in Ethylene Carbonate -Propylene Carbonate (vol. ratio of 1:1) as the electrolyte, and a

Whatman GF/D filter paper acting as the separator. The cyclic voltammetry (CV) tests were performed at a scan rate of 0.1 mV/s with the help of a Keithley Model 2450-EC Source Meter. Galvanometric charge-discharge (GCD) tests and the galvanometric intermittent titration technique (GITT) were carried out using a Neware battery tester (CT-4008T). The rate performance of the samples was evaluated between 0.1C - 6C rates, and the cyclic performance was tested for 200 cycles at a discharge rate of 1C between 1.5 V to 4.2 V. The mass loading for the samples was varied between 2-3 mg/cm², and C-rates were calculated assuming a nominal capacity of 150 mAh/g (assuming a Na⁺ extraction of 0.6). Impedance measurements were performed using a computer-controlled LCR meter (model: ZM 2376, NF Corp.) equipped with an internal DC bias up to 5 V over a 1 Hz – 1 MHz frequency range at room temperature.

3. Results and Discussion

3.1. Structural Characteristics

The Na_{0.75}Mn_{0.75}Ni_{0.25}O₂ (NNM-x; x represents the calcination temperatures) series of materials were synthesized through the sol-gel route with calcination temperatures ranging between 700 to 850 °C followed by furnace cooling. Powder XRD was used to analyze the crystal structure of these samples. The room temperature XRD pattern of each sample and their corresponding Rietveld refinement profiles are depicted in Fig. 1(a) & (c) and Fig. S1. Initial analysis of Fig. 1(a) shows drastic variations in the peaks' positions and intensities, confirming the changes in the crystal structure of the material due to the change in calcination temperature. The Rietveld refinement of the XRD data for the NNM-700 and 750 samples confirms the existence of a single P3 ($R\overline{3}m$ space group) phase, with minor impurities (< 10 wt.%) observed in the former sample. With further increase in synthesis temperature, the P3 (006), (101), (102), (104), and (015) peaks show a gradual decline in intensity in comparison

to P2 (002), (100), (102), (103), (104) diffraction indicating the emergence of a biphasic P2/P3 system with P2 phase becoming dominant with the increase in calcination temperate from 750 °C - 850 °C. The deconvoluted XRD patterns of P2 and P3 phases for NNM-750, 780, and 850 between the 2θ range of 30°- 40° are shown in Fig. 1(c).

The XRD data confirm a continuous conversion of the P3 phase into a P2-type phase with an increase in the calcination temperature and complies with the recent reports in the literature where the P3 phase is regarded as an ordered phase of P2 with lower calcination temperatures [20, 27]. In this investigation, we have synthesized hitherto unknown pure P3 phase in extensively studied Na_{0.75}Mn_{0.75}Ni_{0.25}O₂. More importantly, these XRD results demonstrated that the phase fraction of the P2/P3 biphasic system could be tailored from 0% to 100% simply by controlling the calcination temperature. The crystallographic parameters obtained from Rietveld refinement (Table 1) also show that unit cell volume for P2 (number of formula unit cells in one crystallographic unit cell, Z = 2) and P3 (Z = 3) phases formed at different synthesis temperatures remained essentially unchanged and was found to be around ~80.4 ų and ~121.2 ų, respectively, with similar areas of around 9.51 Ų for the prismatic faces that form the primary Na⁺ migration bottlenecks. The P2 and P3 crystal structures generated using VESTA [43] and output parameters of Rietveld refinement are depicted in Fig. 1(b).

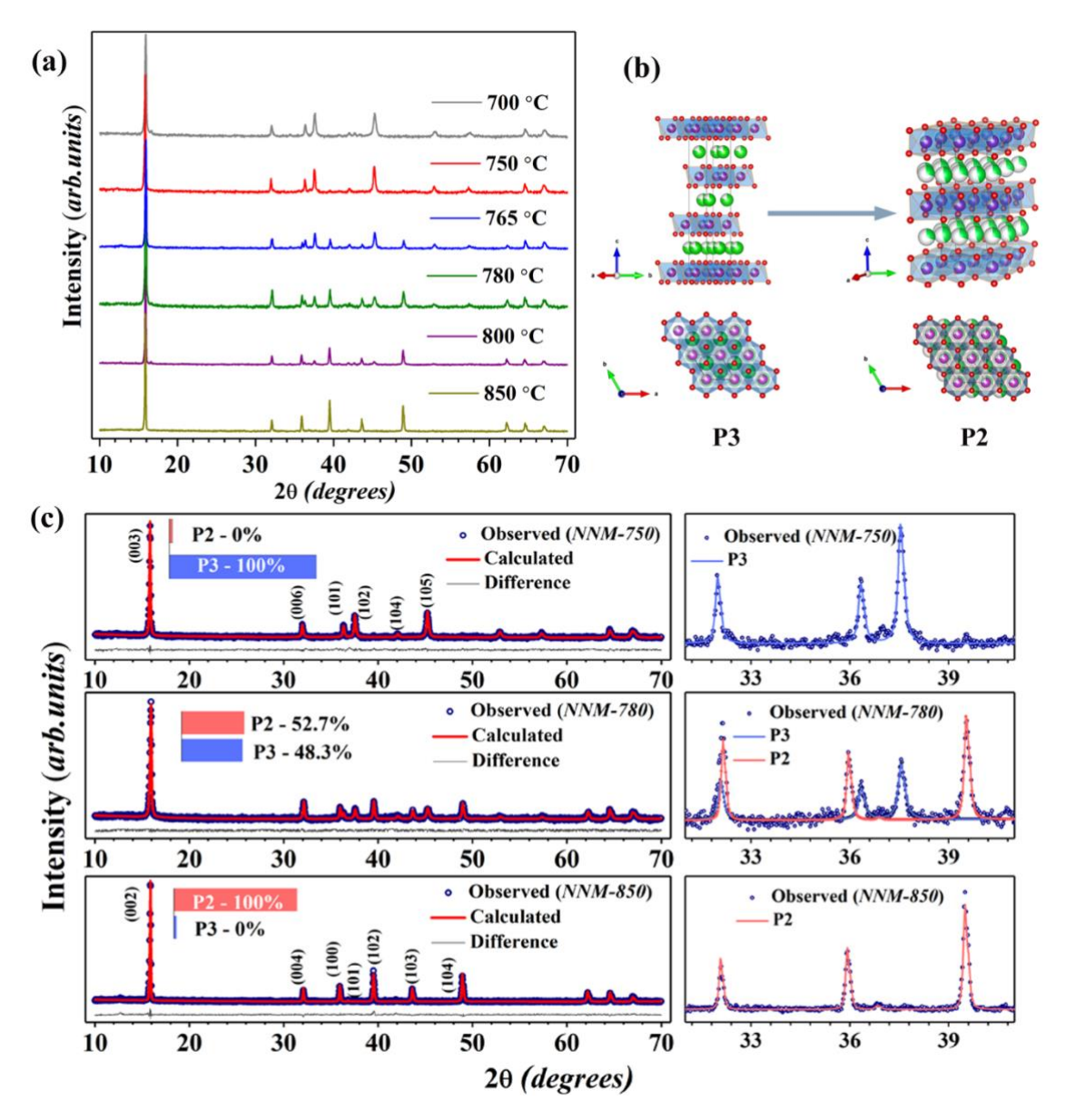


Fig. 1 (a) Phase evolution of Na_{0.75}Mn_{0.75}Ni_{0.25}O₂ with calcination temperature. (b) 2D visualization of P2 and P3 structures generated using VESTA software. (c) Rietveld refinement of XRD data belonging to NNM-750,780, and 850 samples, along with the deconvoluted P2 and P3 phases in the 2θ range of 30-40°.

Another noticeable feature of NNM samples investigated in the present study is the considerable influence of *Na content* on the phase fractions obtained at various calcination temperatures. Figure S2 displays the room temperature XRD patterns of NNM-700, 750 & 800 prepared by adding 5% extra Na. The peaks marked by a * correspond to an O3 phase. This establishes 0.75 as a critical point of Na concentration for obtaining a P2/P3 biphasic

system in Na_{0.75}Mn_{0.75}Ni_{0.25}O₂, above which a tri-phasic system involving P2/P3/O3 starts to form. Interestingly, the temperature at which O3 peaks appeared matched that of the P3 phase formation temperature at ~ 700 °C. With an increase in synthesis temperature, however, the conversion of the P3 phases in the P2 phase continued even in the 5% extra Na samples. At the same time, the relative intensity of the O3 peaks remained the same even after the entire P3 phase had transformed into a P2 phase at 850 °C. Since the main aim of this study was to investigate the structural, electrical, and electrochemical properties of the biphasic P2/P3 system, further characterization of the 5% additional Na samples were not carried out. Detailed investigations involving the effects of Na content in NNM on the structural, electrical, and electrochemical properties will be reported in a future study.

The local structure around the transition metal ions in P3 type NNM-750 and P2 type NNM-850 were probed using fitting of EXAFS data at Mn and Ni K-edge. Figure 2(a-d) represents the . The peaks representing (Mn/Ni)-O and (Mn/Ni)-TM co-ordinations are also marked in the figures. The (Mn/Ni)-O bond lengths obtained from the fit for P2 and P3 type phases matched with those obtained from the Rietveld refinement of XRD data and put the bond lengths at \sim 2 Å The distance between the transition metal ions obtained from the fit in both P2 and P3 type structures were estimated to be around 2.88 Å.

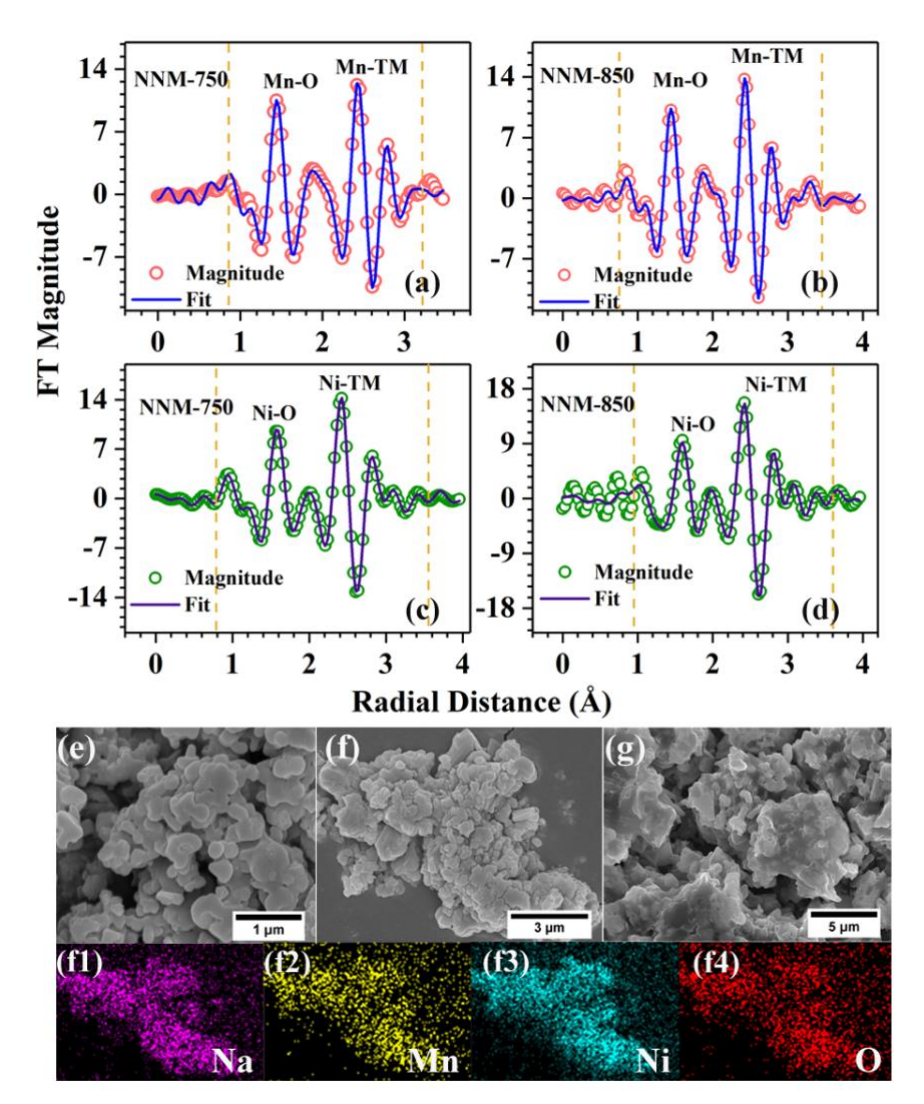


Fig. 2 (a-b) Mn-K edge and (c-d) Ni K edge EXAFS spectra of NNM-750 and NNM-850 samples. SEM micrographs of (e) NNM-750, (f) 780, and (g) 850, along with (f1-4) elemental maps depicting the distribution of the Na, Mn, Ni, and O in NNM-780

Table 1. Lattice parameters of NNM-*x* samples obtained from the Rietveld refinement of room temperature XRD data.

Sample	Phase (Fraction)	a (Å)	c (Å)	$V(\text{Å}^3)$	Reliability Factors
NNM-750	P3 (100%)	2.8866	16.792	121.18	R_{exp} : 2.00
		± 0.0001	$\pm\ 0.002$	± 0.01	R_{wp} : 2.72
	P2 (0%)	-	-	-	R_p : 2.12 GOF : 1.14
NNM-765	P3 (76.7%)	2.8879	16.636	121.07	Rexp: 2.00
	, ,	$\pm~0.0001$	$\pm\ 0.002$	± 0.02	R_{wp} : 2.72
	P2 (23.3%)	2.8864	11.144	80.41	R_p : 2.12
		$\pm~0.0001$	$\pm\ 0.002$	± 0.01	<i>GOF</i> : 1.14
NNM-780	P3 (48.3%)	2.8895	16.771	121.26	Rexp: 2.35
		± 0.0003	± 0.002	± 0.03	$R_{wp}: 2.68$
	P2 (52.7)	2.8874	11.154	80.54	$R_p: 2.12$ GOF: 1.14
		$\pm\ 0.0001$	$\pm\ 0.001$	± 0.01	GOI . 1.14
NNM-800	P3 (28.4%)	2.8887	16.744	121.01	Rexp: 2.11
		$\pm\ 0.0003$	$\pm\ 0.002$	± 0.03	$R_{wp}:2.72$
	P2 (81.6%)	2.8880	11.1493	80.53	$R_p: 2.06$ GOF: 1.28
		$\pm\ 0.0001$	$\pm~0.0006$	± 0.09	GOT . 1.20
NNM-850	P3 (0%)	-	-	-	R _{exp} : 2.85 R _{wp} : 2.15
	P2 (100%)	2.9041	11.1485	80.33	$R_p: 2.19$
		$\pm \ 0.0007$	± 0.0004	$\pm \ 0.01$	GOF: 1.32

The morphology and microstructure of the NNM-*x* samples were studied using FESEM. The representative SEM micrographs of NNM-750, 780, and 850 are displayed in Fig. 2(e-g), and that of NNM-765 and 800 are presented in Fig. S3. The figures show agglomerated and fused particles for samples calcined at 800 °C and 850 °C. In contrast, the samples calcinated at temperatures below 800 °C have smaller particles with better-defined contours and facets.

The elemental map of NNM-780 portrayed in Fig. 2(f1-f4) shows the homogeneous distribution of all the constituent elements.

The microstructure of a cathode material is a significant factor in determining its GCD rate performance. Samples with smaller and lesser agglomerated particles usually show higher specific capacities (especially at higher discharge rates) than those with larger and fused particles. This is because liquid electrolytes typically have much higher ionic conductivities than cathode materials; hence, a porous cathode layer with smaller particles effectively provides a shorter diffusion path for Na-ions than a cathode with larger and highly agglomerated particles [44, 45]. The effect of particle sizes is not so apparent at low discharge rates (~ 0.1C) but becomes a deterministic factor in boosting specific capacity at higher discharge rates. Hence, even though the available literature on layered oxides suggests a higher value of Na⁺ diffusion coefficient for P2-type materials compared to P3-types, the higher concentration of fused particles observed in the P2-dominated NNM-800 and NNM-850 samples could lower their specific capacities at high discharge rates (inferior rate performance) compared to the P3 dominated samples NNM-750 and 780 samples.

XPS spectra of the NNM-750, and 850 samples were acquired to determine the valence states of their constituent elements and are shown in Fig. 3, along with the fitted data. The Ni 2p spectra show 2 coupled peaks at 854.26 and 871.75 eV, which suggests the presence of Ni²⁺ ions [23, 46, 47]. The O 1s spectra show the presence of adsorbed CO₂ along with bonded oxygen in the LO. The Mn 2p XPS spectra can be deconvoluted into 4 peaks: at 641.8 & 653.2 eV belonging to Mn³⁺, 643.2 & 654.7 eV corresponding to Mn⁴⁺, indicating a mixed valence state of Mn-ions in 3+ and 4+ oxidation states in these samples [23, 46, 47]. The X-ray absorption near edge structure spectra (XANES) of NNM-750 and 850 at Mn and Ni K-edge, depicted in Fig. S4, also show similar energy levels for Mn and Ni ions for both

samples. The XANES and XPS spectra of both samples are almost identical, suggesting that Na volatilization during the NNM-*x* series synthesis was negligible. This also indicates that the phase transformation of NNM from a P3-type to a P2-type upon increasing the calcination temperature from 750 °C to 850 °C is not guided by the starvation of Na-ion within the structure (due to Na volatilization) and both the P3 and P2 type cathodes contained a similar concentration on Na-ions.

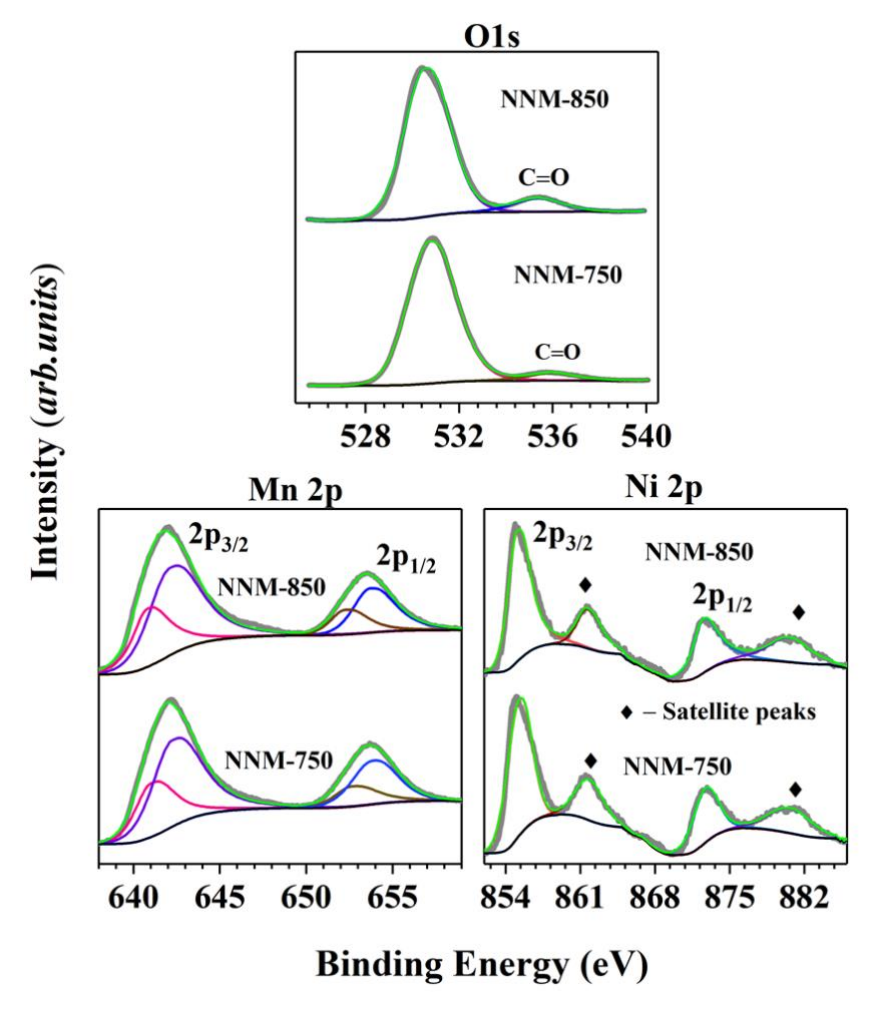


Fig. 3 XPS spectra of NNM-750 and NNM-850.

3.2. Electrochemical Characteristics

The electrochemical characterization of NNM-x samples was evaluated in a coin cell configuration, cycled between 1.5 and 4.2 V. Figure 4 shows the cyclic voltammograms of

NNM-750, 780, and 850 and the same for NNM-765 and NNM-800 are displayed in Fig. S5. The redox peaks observed below 3 V in the cyclic voltammograms are attributed to the Mn^{3+/4+} redox process [48, 49], while the peaks in 3.0 V – 3.5 V and 3.5 V - 4.0 V ranges indicate the activity of Ni^{2+/3+} and Ni^{3+/4+} couples, respectively [50, 51]. Interestingly in the NNM-750 sample, containing a pure P3 phase, the CV curve shows only 3 pairs of distinct peaks at 2.35/1.79 V, 3.50/3.00 V, and 3.92/3.35 V. An increased number of peaks are observed in the CV curves for P2 dominated NNM-800, 850 samples, possibly due to Na⁺ vacancy ordering in P2-type materials as reported in the literature [48, 52]. The relatively lower concentration of Na-ion vacancy ordering peaks in the other P3 dominant samples points to an innate ability of the P3-type phase to suppress Na-ion vacancy ordering. This could reflect higher rate performance and cyclic stability in the P3 dominant samples, as ordering of Na-ion vacancies is known to induce severe structural transitions that degrade electrochemical performance.

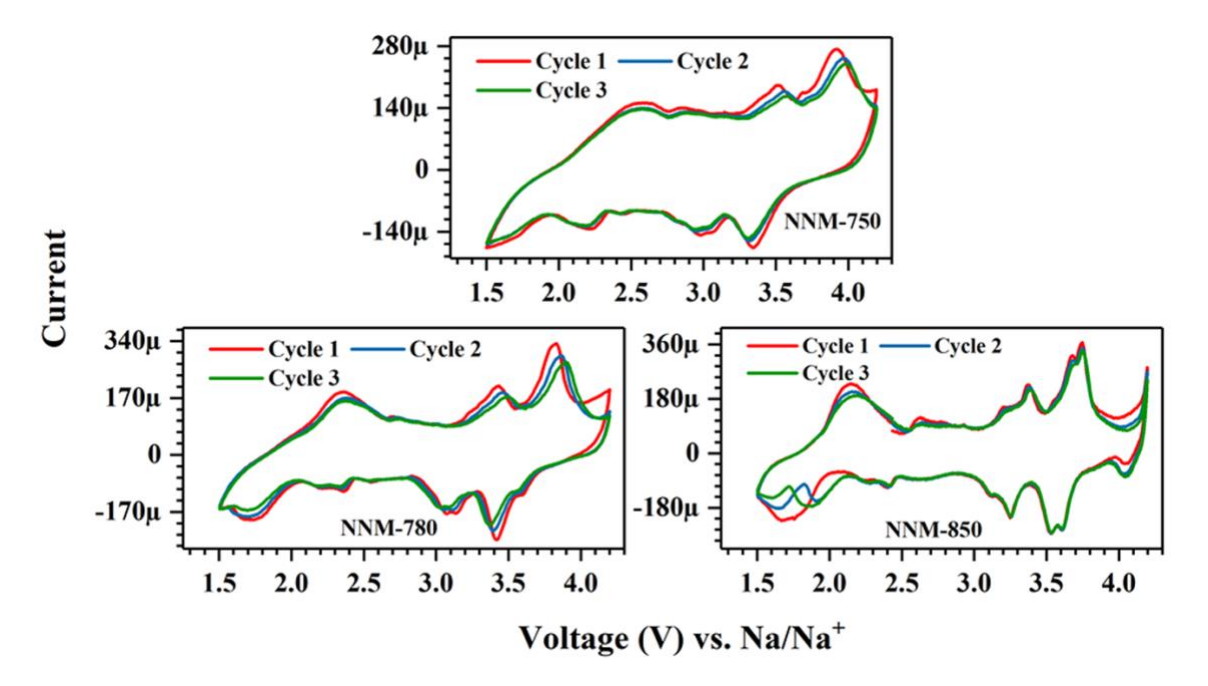


Fig. 4 Cyclic voltammograms of NNM-750, 780; and 850 samples.

The galvanostatic charge-discharge curves of NNM-x half cells obtained at different C rates are displayed in Fig. 5(a). As expected, the GCD curves for all the samples show multiple

plateaus relating to different redox couples at voltage ranges identified in their respective cyclic voltammograms. To further analyze the charge/discharge performance of the cathodes, the dQ/dV vs. voltage (V) plots were obtained for all samples at 0.1C. The dQ/dV vs. V plots (Fig. 5(b)) reveal an interesting trend: ΔV between corresponding oxidation and reduction peaks decreases from ~ 0.2 V for NNM-750 (with a single P3 phase) sample to ~ 0.05 V for NNM-780 (with a biphasic P2/P3 structure). This could be due to the multiple phase transformations occurring in the cathode which lowers diffusion coefficient of Na-ions and increases the polarisation voltage. With the introduction of the P2 phase in the NNM-760 and NNM-780 samples ΔV reduces considerably suggesting better stabilisation of the structure in the biphasic cathodes. In contrast, a higher ΔV of almost 0.15 V in P2 phase dominant NNM-800 and NNM-850 samples may result from their particle morphologies (fused and agglomerated particles, as reported in the microstructural section). The lower polarisation potentials of biphasic cathodes also enabled higher energy efficiencies of \sim 85% compared to \sim 75% in the P3-type cathodes. This is depicted in the GCD curves of the NNM-750 (Fig. S6), with the portion shaded in red representing energy loss.

Another striking feature of GCD curves (Fig. 5(a)) is the decrease in the specific capacity of the NNM-*x* cathodes with an increase in P2 concentration at a charge/discharge rate of 0.1C. The specific capacity decreases from 190 mAh g⁻¹ in the NNM-750 to 180 mAh g⁻¹ in NNM-765, 172 mAh g⁻¹ in NNM-780, and further to 155 mAh g⁻¹ for the NNM-850. This corresponds to the extraction/insertion of about 0.8 Na-ions in the monophasic P3 sample, which drops to 0.65 Na-ions in the NNM-850 cathode. The higher amount of Na-ions required during cycling of the P3 type cathode is obtained from the Na metal anode during the discharge process. It is important to keep in mind that the as-synthesized NNM-750 contains only 0.75 Na-ions per formula unit cell, assuming a final concentration of Na_{0.15}Mn_{0.75}Ni_{0.25}O₂ at the end of charging, a deficiency of 0.25 Na ions need to be

compensated to obtain a capacity of 190 mAh/g. Hence, in a full-cell configuration, the P3type cathode cannot deliver the same specific capacity. Accordingly, other synthesis techniques should be explored to stabilize Na-rich P3-type structures. The decreasing trend in specific capacity with the increase in P2 concentration is also expected. It confirms often theorized speculations in the literature about a thermodynamically synthesized P3-type phase being able to accommodate higher amounts of Na ions within its structure than its P2 counterpart. With the increase in C rate (Fig. 5(c)), the P3 dominant samples start to underperform, losing about 60% of their capacity at 0.1C to reach about 74 mAh g⁻¹ at 1C, which then lowers to only ~ 5 mAh g⁻¹ at 6C. In contrast, NNM-765 and 780 cathodes show incredible rate performance, with their specific capacities reaching 122 mAh g⁻¹ and 130 mAh g⁻¹ at 1C, representing a fading of only about 32% and 23% of their capacities at 0.1C. Even with a charge/discharge rate of 6C, these cathodes exhibited a capacity of about 82 mAh g⁻¹ and 97 mAh g⁻¹, respectively. Such high-rate performance makes these samples attractive for stationary and portable storage applications. The lower rate performance of the P3 represents a poor Na-ion diffusion coefficient of the material, possibly due to rapid phase conversions that do not support a fast transport of Na-ions. Incorporating a P2 phase may have been responsible for opening up better Na⁺ conducting pathways within the material and preventing unwanted phase transitions resulting in greater extraction of Na⁺ even at high C rates in the NNM-765&780 cathodes. On the other hand, the lower rate performance observed for NNM-800 and NNM-850 samples (where specific capacities drop from around 155 mAh g⁻¹ at 0.1C to about 74 mAh g⁻¹ and 64 mAh g⁻¹ at 1C, respectively) could be resulting from agglomerated & fused particle morphologies caused by higher calcination temperatures that increase the overall diffusion path for Na-ions in cathode layer.

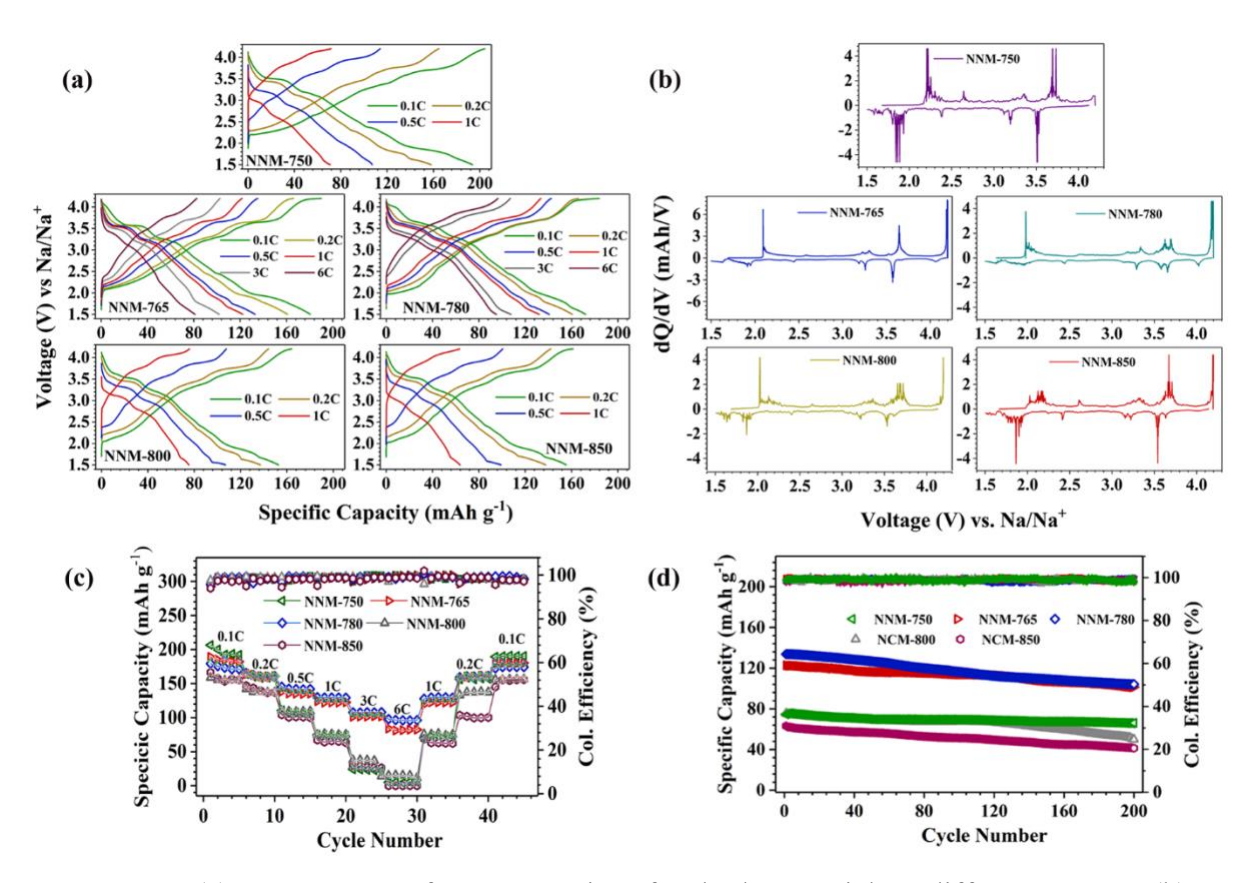


Fig. 5 (a) GCD curves of NNM-*x* series of cathode materials at different C rates. (b) dQ/dV vs. voltage (V) plots of NNM-*x* cathodes at a discharge rate of 0.1C. (c) Rate performance and (d) cyclic stability of NNM-*x* cathodes at a discharge rate of 1C.

Figure 5(d) illustrates the cyclic performance of the NNM-*x* cathodes at a charge/discharge rate of 1C between 1.5 V - 4.2 V. The cyclic data indicates the monophasic P3 cathode to have the highest capacity retention of ~ 90% after 200 cycles. On the other hand, the high-performing NNM-765 and 780 show a specific capacity of 97 mAh g⁻¹ and 104 mAh g⁻¹, respectively, after 200 cycles which is close to 83% and 80% of their initial capacity at 1C. The poor cyclic performance of the NNM-800 & NNM-850 cathodes (only 65 % capacity retention after 200 cycles) was expected as the detrimental effects of activating Mn^{3+/4+} on the P2 structure in the Na-Mn-Ni system is well reported in the literature due to the presence of Jahn-Teller active Mn³⁺ below 2 V [38, 53]. Early signs of structural instability in these compounds with the introduction of Mn³⁺ can be inferred from their GCD curves (Fig. 5(a)),

where a notch-like feature caused by the sudden change in slope is visible at 1.7 V. The Nyquist plots of NNM-750, 780 and 850 cells illustrated in Fig. S7 also concur with the cyclic data where after 200 charge/discharge cycles NNM-850 cell showed an increased resistance of 1150 Ω , which is almost twice as that of the 550 Ω in NNM-780.

Compared to the P2 phase, the P3 structure seems to be resilient to the structural distortions induced by the Mn³+. The resilience of the P3-type structure in maintaining its structural integrity even after undergoing multiple phase transitions may have also been aided by its smaller particle size and lower degrees of agglomeration, allowing each particle to expand and contract freely without generating a high degree of stress. Further, the widely reported synergistic effects found in biphasic layered oxides prevent each other from undergoing structural transformations during cycling and may have also contributed to the higher cyclic stability of NNM-780 [26, 27, 31, 32].

The Na-ion diffusion kinetics for the NNM-x samples were investigated using the galvanostatic intermittent titration technique (GITT) between 1.5 to 4.2 V. The technique involves applying a constant current pulse for 10 minutes, followed by a dwell time, during which the cell is allowed to reach a quasi-equilibrium state. This process is repeated till the cut-off voltages are reached. Figure S8 shows the GITT charge-discharge curves for the NNM-x samples. The Na⁺ diffusion inside the cathode material is assumed to obey Fick's first law, and the Na⁺ diffusion coefficient (D_{Na^+}) can be calculated using the following Eq.1.

$$D_{Na^{+}} = \frac{4}{\pi \tau} \left(\frac{m_B V_m}{M_B S}\right)^2 \left(\frac{\Delta E_S}{\Delta E_{\tau}}\right)^2 \tag{1}$$

Here, M_B and V_m represent the molar mass and molar volume of the cathode material, m_B is the mass of active material, τ is the time of a single constant current pulse, and S denotes the active surface area of the electrode. ΔE_S and ΔE_{τ} represent the change of the steady-state

voltage and the voltage change during the constant current pulse, respectively. Figure 6 shows the variation of D_{Na}⁺ of NNM-x with voltage. Unsurprisingly NNM-765 and 780 cathodes showed the highest diffusion coefficient of 1 ×10⁻¹⁰ and 7.6 ×10⁻¹⁰ cm²s⁻¹, respectively, while the NNM 750 & 850 showed the lowest diffusion coefficients close to 4 ×10⁻¹⁰ cm²s⁻¹. All NNM-x cathodes show slow diffusion kinetics at the start of a charge and discharge process. The lower diffusion coefficients at the outset of the charging are due to a larger concentration of Na-ions within the structure, causing starvation of Na-ion vacancies. In contrast, a higher number of Na-ion vacancies may have led to sluggish Na-ion diffusion kinetics at the initial phase of the discharge process. The Na-ion diffusion coefficient also shows lower variations in the P2 type structure which points to its excellent structure stability throughout the charge-discharge process, while larger variations in the P3 containing cathodes, especially at voltages where a peak is observed in their corresponding dQ/dV vs. V plots, may be due to structural variations within the P3 type structure. Nevertheless, the decline in the intensity of these variations and higher diffusion coefficients in NNM-765 and NNM-780 cathodes aligns with the observations from the GCD rate performance curves on the importance of the P2 phase enhancing Na⁺ diffusion through the material.

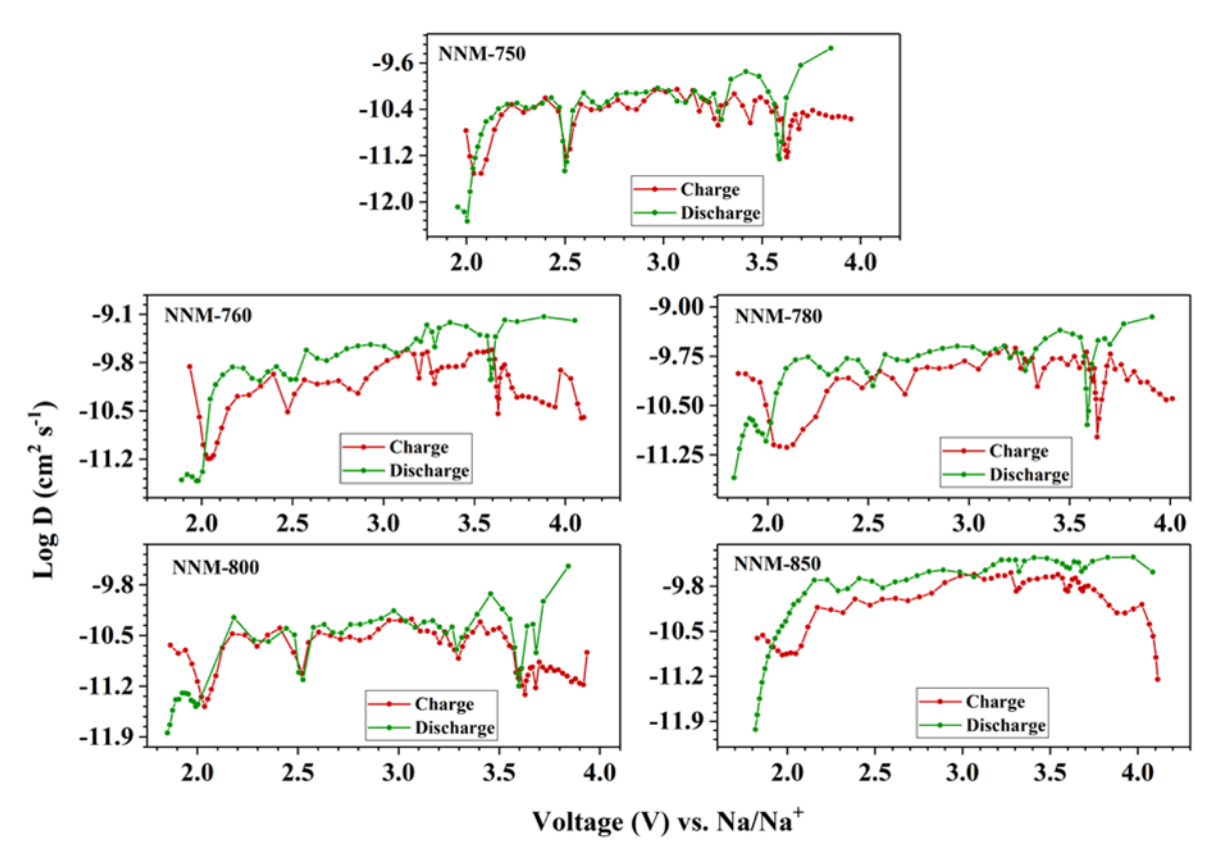


Fig. 6 Variation of diffusion coefficients of NNM-*x* cathodes during charging and discharging.

3.3. Operando Synchrotron XRD studies

Many of the speculations regarding the varied electrochemical performance of the P3-type NNM-750 and other biphasic cathodes can be confirmed through the *operando* synchrotron XRD studies of NNM-750 (Fig. 7) and NNM-780 (Fig. S9) cathodes. The *operando* SXRD patterns of NNM-750 portray the structural evolution of the P3 phase during a charge/discharge cycle. Apart from the apparent shifting of the P3 (003) peak (Fig. 7(b)) towards higher angles during discharge and the appearance of an O3 phase at lower voltages (~ below 2.5 V), the emergence of a new but subtle O'3 phase in P3-type NNM-750 at voltages below 3.6 V (Fig. 7(b1)) is an important development [32, 50, 51]. This phase appears at about ~3.6 V during the discharge cycle and persists throughout the discharge process, even after the entire P3 is converted into an O3 phase (at about 2 V, as shown in Fig.

7(b1 & c). However, during the charging cycle, the O'3 peaks coalesce with the existing P3 peaks. The emergence of the O'3 phase at 3.6 V during discharge and its coalescence with the P3 phase at 3.2 V would explain the increase in polarisation potential observed from the dQ/dV vs. V plots, especially at higher voltages, where Ni^{2+/3+} and Ni^{3+/4+} redox couples are active. During the charging cycle, the Na ions are extracted from a pure P3 phase at the characteristic oxidation potential of Ni²⁺ to 3+ & 4+ oxidation states, which will be vastly different from the potential required to reduce the Ni⁴⁺ to 2+ oxidation state in the P3/O'3 biphasic system developed during the discharge process, widening the potential gap between the two redox processes. The existence of the O'3 phase alongside the P3 and O3 phases for extended voltage windows could also explain the poor rate performance exhibited by NNM-750, as the distorted monoclinic O'3 phase shows slower Na ion transport properties. In comparison, the number of structural transformations in the biphasic NNM-780 sample appears to be limited. The operando SXRD patterns do not show any changes to the P2 type structure throughout the discharge process, while only a partial conversion of the P3 to O3 phase conversion is observed, possibly due to the synergetic effect of the P2/P3 system [26, 27, 31, 32]. No evidence of the P2 - OP4 phase transformation (often reported in the literature) during charging (in the 2.0 to 4.2 V range) or the P3→O'3 transformation is observed in the SXRD plots, suggesting high structural stability of the material. The endurance of its structure towards phase transformations and the coexistence of highly conducting P2 & P3 phases throughout most of its charge-discharge process has resulted in the superior cyclic stability and rate performance exhibited by NNM-780.

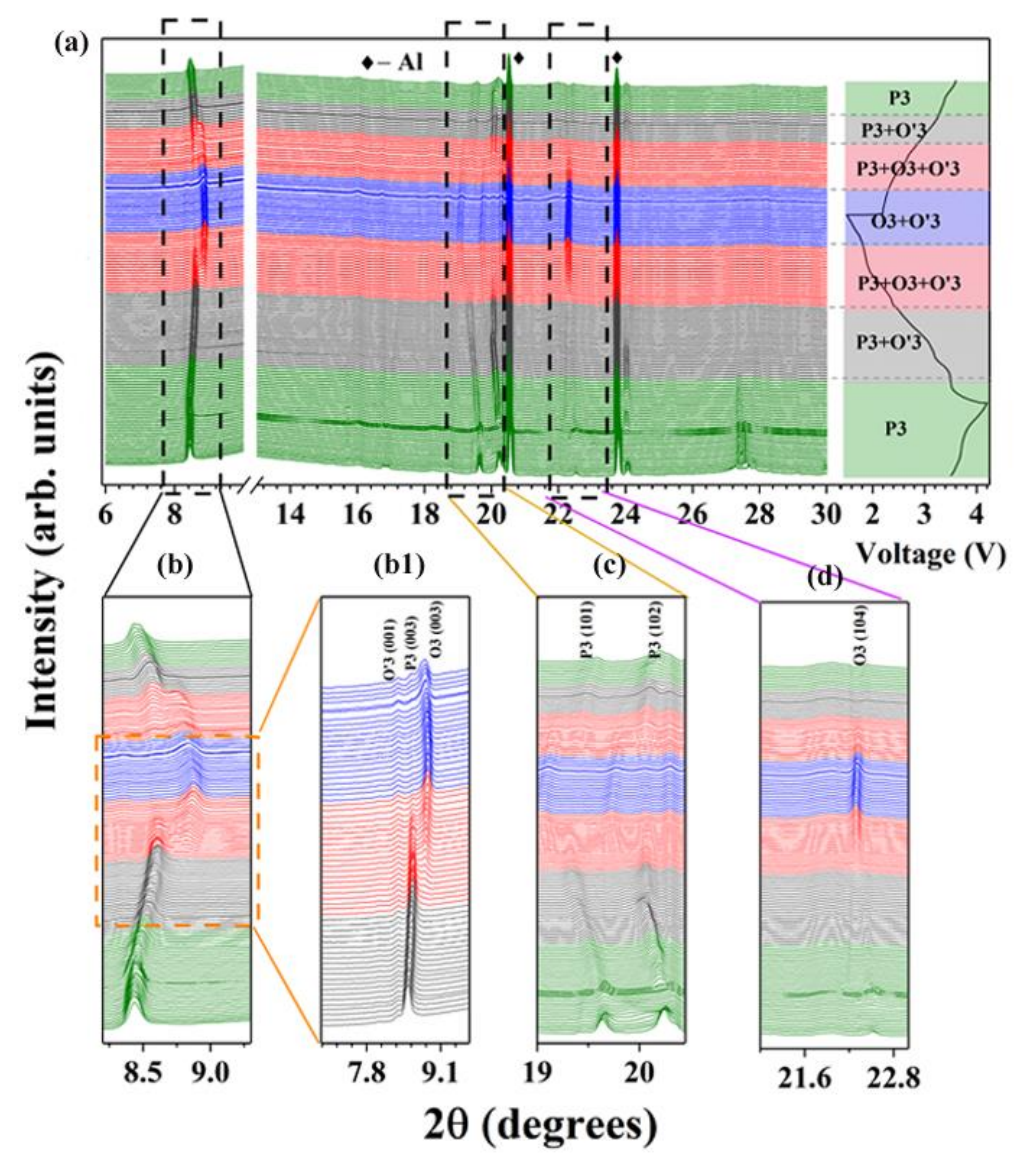


Fig. 7 (a) *Operando* Synchrotron x-ray diffraction patterns of NNM-750 obtained during galvanostatic charge/discharge process at 0.1C with (b-d) displaying zoomed views in the vicinity of the marked regions.

4. Conclusions

Room temperature XRD plots of the NNM-x series of cathodes have demonstrated the dependence of P2 and P3 phase fractions on the synthesis temperature. P3 phase formation was found to occur at around 700 °C while the P3 to P2 transformation process was observed at calcination temperatures above 750 °C. This was exploited to obtain a series of cathode materials based on Na_{0.75}Mn_{0.75}Ni_{0.25}O₂ with varying P2/P3 phase concentrations. The

conversion of P3 to P2-type single phase upon increasing the calcination temperature from 750 °C to 850 °C, with P2/P3 biphasic structures at intermediate temperatures, was confirmed by the Rietveld refinement of the x-ray diffraction (XRD) data. SEM micrographs of the materials revealed that the lower calcination temperatures of P3 dominant NNM-750, 765, and 780 were beneficial in preventing particle agglomeration, which was later confirmed to play a key role in enhancing their rate performance and cyclic stability. Electrochemical tests on the NNM-x series of cathodes showed specific capacity peaking at 190 mAh/g in NNM-750 (pure P3-type cathode) and steadily degrading with the increasing P2 concentration, reaching 154 mAh/g in NNM-850 (the pure P2-type cathode) in an electrochemical window of 1.5 - 4.2 V. In terms of rate performance, NNM-780 and 765 cathodes exhibited specific capacities close to 97 mAh/g and 82 mAh/g at 6C. The monophasic NNM-750 and the biphasic NNM-765 & 780 also showed superior cyclic stability by retaining about 90% and 80% of their initial specific capacity after 200 cycles at a discharge rate of 1C between 1.5 -4.2 V, which makes them ideal for stationary storage applications. *Operando* SXRD studies on NNM-750 showed that the cathode material underwent multiple phase transitions from a P3 to O'3+O3 phase during the charge/discharge cycle, which may have limited its rate performance. The operando SXRD plots of NNM-780, on the other hand, showed only a partial conversion of the P3 phase to the O3 phase at lower voltages with little to no changes in the P2 structure during cycling. The excellent structural stability of the biphasic cathode material is attributed to the synergistic effect of the coexistence of the P2 and P3 phases. The superior rate performance exhibited by these cathodes is also owed to the ability to retain highly conducting P2 and P3 phases for most of the charge/discharge process.

Acknowledgements

SK thanks the Science and Engineering Research Board (SERB), Govt. of India, for the financial support (grant number: CRG/2021/005548). The authors acknowledge DST and Dr. S. N. Jha for his help in recording the EXAFS spectra at RRCAT, Indore, India.

Declaration of Interest

The authors declare no conflict of interests.

References

- [1] D. Buchholz, A. Moretti, R. Schmuch, S. Nowak, S. V, W. M, S. Passerini, Towards Naion batteries Synthesis and Characterization of a novel high capacity Na-ion intercalation material, Chem. Inform, 160 (2013) 44 https://doi.org/10.1002/chin.201319014
- [2] J. Darga, J. Lamb, A. Manthiram, Industrialization of Layered Oxide Cathodes for Lithium-Ion and Sodium-Ion Batteries: A Comparative Perspective, Energy Technol., 8 (2020) 2000723 https://doi.org/10.1002/ente.202000723
- [3] R.J. Clément, P.G. Bruce, C.P. Grey, Review—Manganese-Based P2-Type Transition Metal Oxides as Sodium-Ion Battery Cathode Materials, J. Electrochem. Soc., 162 (2015) A2589-A2604 https://doi.org/10.1149/2.0201514jes
- [4] R. Usiskin, Y. Lu, J. Popovic, M. Law, P. Balaya, Y.-S. Hu, J. Maier, Fundamentals, status and promise of sodium-based batteries, Nature Rev. Mater., 6 (2021) 1020-1035 https://doi.org/10.1038/s41578-021-00324-w
- [5] Y.-F. Zhu, Y. Xiao, S.-X. Dou, Y.-M. Kang, S.-L. Chou, Spinel/Post-spinel engineering on layered oxide cathodes for sodium-ion batteries, eScience, 1 (2021) 13-27 https://doi.org/10.1016/j.esci.2021.10.003
- [6] L. Qiao, X. Judez, T. Rojo, M. Armand, H. Zhang, Review—Polymer Electrolytes for Sodium Batteries, J. Electrochem. Soc., 167 (2020) 070534 https://doi.org/10.1149/1945-7111/ab7aa0
- [7] Mineral commodity summaries 2021, Mineral Commodity SummariesReston, VA, 2021, pp. 200.
- [8] C. Vaalma, D. Buchholz, M. Weil, S. Passerini, A cost and resource analysis of sodiumion batteries, Nature Rev. Mater., 3 (2018) 18013 https://doi.org/10.1038/natrevmats.2018.13
 [9] J. Peters, A. Cruz, M. Weil, Exploring the Economic Potential of Sodium-Ion Batteries,

Batteries, 5 (2019) 10 https://doi.org/10.3390/batteries5010010

- [10] J.-Y. Hwang, S.-T. Myung, Y.-K. Sun, Sodium-ion batteries: present and future, Chem. Soc. Rev., 46 (2017) 3529-3614 https://doi.org/10.1039/C6CS00776G
- [11] X. Xiang, K. Zhang, J. Chen, Recent Advances and Prospects of Cathode Materials for Sodium-Ion Batteries, Adv. Mater., 27 (2015) 5343-5364 https://doi.org/10.1002/adma.201501527
- [12] D. Kundu, E. Talaie, V. Duffort, L.F. Nazar, The Emerging Chemistry of Sodium Ion Batteries for Electrochemical Energy Storage, Angew. Chem. Int. Ed., 54 (2015) 3431-3448 https://doi.org/10.1002/anie.201410376
- [13] R. Thirupathi, V. Kumari, S. Chakrabarty, S. Omar, Recent progress and prospects of NASICON framework electrodes for Na-ion batteries, Prog. Mater Sci., 137 (2023) 101128 https://doi.org/10.1016/j.pmatsci.2023.101128
- [14] H.N. Vasavan, M. Badole, S. Saxena, A.K. Das, S. Deswal, P. Kumar, S. Kumar, Excellent Structural Stability-Driven Cyclability in P2-Type Ti-Based Cathode for Na-Ion Batteries, ACS Appl. Energy Mater., 6 (2023) 2440-2447 https://doi.org/10.1021/acsaem.2c03750
- [15] S. Saxena, H.N. Vasavan, M. Badole, A.K. Das, S. Deswal, P. Kumar, S. Kumar, Tailored P2/O3 phase-dependent electrochemical behavior of Mn-based cathode for sodiumion batteries, Journal of Energy Storage, 64 (2023) 107242 https://doi.org/10.1016/j.est.2023.107242
- [16] E. Goikolea, V. Palomares, S. Wang, I.R. de Larramendi, X. Guo, G. Wang, T. Rojo, Na-Ion Batteries—Approaching Old and New Challenges, Adv. Energy Mater., 10 (2020) 2002055 https://doi.org/10.1002/aenm.202002055
- [17] C. Delmas, C. Fouassier, P. Hagenmuller, Structural classification and properties of the layered oxides, Physica B+C, 99 (1980) 81-85 https://doi.org/10.1016/0378-4363(80)90214-4

- [18] F. Wei, Q. Zhang, P. Zhang, W. Tian, K. Dai, L. Zhang, J. Mao, G. Shao, Review—Research Progress on Layered Transition Metal Oxide Cathode Materials for Sodium Ion Batteries, J. Electrochem. Soc., 168 (2021) 050524 https://doi.org/10.1149/1945-7111/abf9bf [19] X. Liang, T.-Y. Yu, H.-H. Ryu, Y.-K. Sun, Hierarchical O3/P2 heterostructured cathode materials for advanced sodium-ion batteries, Energy Storage Mater., 47 (2022) 515-525 https://doi.org/10.1016/j.ensm.2022.02.043
- [20] L. Zhang, J. Wang, J. Li, G. Schuck, M. Winter, G. Schumacher, J. Li, Preferential occupation of Na in P3-type layered cathode material for sodium ion batteries, Nano Energy, 70 (2020) 104535 https://doi.org/10.1016/j.nanoen.2020.104535
- [21] Z. Liu, X. Xu, S. Ji, L. Zeng, D. Zhang, J. Liu, Recent Progress of P2-Type Layered Transition-Metal Oxide Cathodes for Sodium-Ion Batteries, Chem. Eur. J., 26 (2020) 7747-7766 https://doi.org/10.1002/chem.201905131
- [22] C. Zhao, Z. Yao, Q. Wang, H. Li, J. Wang, M. Liu, S. Ganapathy, Y. Lu, J. Cabana, B. Li, X. Bai, A. Aspuru-Guzik, M. Wagemaker, L. Chen, Y.-S. Hu, Revealing High Na-Content P2-Type Layered Oxides as Advanced Sodium-Ion Cathodes, J. Am. Chem. Soc., 142 (2020) 5742-5750 https://doi.org/10.1021/jacs.9b13572
- [23] W. Kang, D.Y.W. Yu, P.-K. Lee, Z. Zhang, H. Bian, W. Li, T.-W. Ng, W. Zhang, C.-S. Lee, P2-Type Na_xCu_{0.15}Ni_{0.20}Mn_{0.65}O₂ Cathodes with High Voltage for High-Power and Long-Life Sodium-Ion Batteries, ACS Appl. Mater. Interfaces, 8 (2016) 31661-31668 https://doi.org/10.1021/acsami.6b10841
- [24] H. Guo, M. Avdeev, K. Sun, X. Ma, H. Wang, Y. Hu, D. Chen, Pentanary transition-metals Na-ion layered oxide cathode with highly reversible O3-P3 phase transition, Chem. Eng. J., 412 (2021) https://doi.org/10.1016/j.cej.2021.128704

- [25] L. Xian, M. Li, D. Qiu, C. Qiu, C. Yue, F. Wang, R. Yang, P3-type layered Na_{0.26}Co_{1-x}Mn_xO₂ cathode induced by Mn doping for high-performance sodium-ion batteries, J. Alloys Compd., 905 (2022) 163965 https://doi.org/10.1016/j.jallcom.2022.163965
- [26] C. Hakim, H.D. Asfaw, R. Younesi, D. Brandell, K. Edström, I. Saadoune, Development of P2 or P2/P3 cathode materials for sodium-ion batteries by controlling the Ni and Mn contents in Na_{0.7}Co_xMn_yNi_zO₂ layered oxide, Electrochim. Acta, 438 (2023) 141540 https://doi.org/10.1016/j.electacta.2022.141540
- [27] Y.-N. Zhou, P.-F. Wang, Y.-B. Niu, Q. Li, X. Yu, Y.-X. Yin, S. Xu, Y.-G. Guo, A P2/P3 composite layered cathode for high-performance Na-ion full batteries, Nano Energy, 55 (2019) 143-150 https://doi.org/10.1016/j.nanoen.2018.10.072
- [28] J. Liu, C. Didier, M. Sale, N. Sharma, Z. Guo, V.K. Peterson, C.D. Ling, Elucidation of the high-voltage phase in the layered sodium ion battery cathode material P3–Na_{0.5}Ni_{0.25}Mn_{0.75}O₂, J. Mater. Chem. A, 8 (2020) 21151-21162 https://doi.org/10.1039/D0TA06600A
- [29] A. Tripathi, S. Xi, S.R. Gajjela, P. Balaya, Introducing Na-sufficient P3-Na_{0.9}Fe_{0.5}Mn_{0.5}O₂ as a cathode material for Na-ion batteries, Chem. Commun., 56 (2020) 10686-10689 https://doi.org/10.1039/D0CC03701J
- [30] T. Risthaus, L. Chen, J. Wang, J. Li, D. Zhou, L. Zhang, D. Ning, X. Cao, X. Zhang, G. Schumacher, M. Winter, E. Paillard, J. Li, P3 Na_{0.9}Ni_{0.5}Mn_{0.5}O₂ Cathode Material for Sodium Ion Batteries, Chem. Mater., 31 (2019) 5376-5383 https://doi.org/10.1021/acs.chemmater.8b03270
- [31] Y.-N. Zhou, Z. Xiao, D. Han, S. Wang, J. Chen, W. Tang, M. Yang, L. Shao, C. Shu, W. Hua, D. Zhou, Y. Wu, Inhibition of the P3–O3 phase transition via local symmetry tuning in P3-type layered cathodes for ultra-stable sodium storage, J. Mater. Chem. A, 11 (2023) 2618-2626 https://doi.org/10.1039/D2TA09277H

- [32] E. Lee, J. Lu, Y. Ren, X. Luo, X. Zhang, J. Wen, D. Miller, A. DeWahl, S. Hackney, B. Key, D. Kim, M.D. Slater, C.S. Johnson, Layered P2/O3 Intergrowth Cathode: Toward High Power Na-Ion Batteries, Adv. Energy Mater., 4 (2014) 1400458 https://doi.org/10.1002/aenm.201400458
- [33] Y. Chen, G. Su, X. Cheng, T. Du, Y. Han, W. Qiang, B. Huang, Electrochemical performances of P2-Na_{2/3}Ni_{1/3}Mn_{2/3}O₂ doped with Li and Mg for high cycle stability, J. Alloys Compd., 858 (2021) 157717 https://doi.org/10.1016/j.jallcom.2020.157717
- [34] Z. Lu, J.R. Dahn, In Situ X-Ray Diffraction Study of P2-Na_{2/3}[Ni_{1/3}Mn_{2/3}]O₂, J. Electrochem. Soc., 148 (2001) A1225 https://doi.org/10.1149/1.1407247
- [35] P. Manikandan, D. Ramasubramonian, M.M. Shaijumon, Layered P2-type Na_{0.5}Ni_{0.25}Mn_{0.75}O₂ as a high performance cathode material for sodium-ion batteries, Electrochim. Acta, 206 (2016) 199-206 https://doi.org/10.1016/j.electacta.2016.04.138
- [36] J.W. Somerville, A. Sobkowiak, N. Tapia-Ruiz, J. Billaud, J.G. Lozano, R.A. House, L.C. Gallington, T. Ericsson, L. Häggström, M.R. Roberts, U. Maitra, P.G. Bruce, Nature of the "Z"-phase in layered Na-ion battery cathodes, Energy Environ. Sci., 12 (2019) 2223-2232 https://doi.org/10.1039/C8EE02991A
- [37] H. Liu, X. Gao, J. Chen, J. Gao, S. Yin, S. Zhang, L. Yang, S. Fang, Y. Mei, X. Xiao, L. Chen, W. Deng, F. Li, G. Zou, H. Hou, X. Ji, Reversible OP4 phase in P2–Na_{2/3}Ni_{1/3}Mn_{2/3}O₂ sodium ion cathode, J. Power Sources, 508 (2021) 230324 https://doi.org/10.1016/j.jpowsour.2021.230324
- [38] H.N. Vasavan, M. Badole, S. Dwivedi, D. Kumar, P. Kumar, S. Kumar, Enhanced rate performance and specific capacity in Ti-substituted P2-type layered oxide enabled by crystal structure and particle morphology modifications, Chem. Eng. J., 448 (2022) 137662 https://doi.org/10.1016/j.cej.2022.137662

- [39] L. Yang, S.-h. Luo, Y. Wang, Y. Zhan, Q. Wang, Y. Zhang, X. Liu, W. Mu, F. Teng, Cu-doped layered P2-type Na_{0.67}Ni_{0.33-x}Cu_xMn_{0.67}O₂ cathode electrode material with enhanced electrochemical performance for sodium-ion batteries, Chem. Eng. J., 404 (2020) 126578 https://doi.org/10.1016/j.cej.2020.126578
- [40] L. Yu, Z. Cheng, K. Xu, Y.-X. Chang, Y.-H. Feng, D. Si, M. Liu, P.-F. Wang, S. Xu, Interlocking biphasic chemistry for high-voltage P2/O3 sodium layered oxide cathode, Energy Storage Mater., 50 (2022) 730-739 https://doi.org/10.1016/j.ensm.2022.06.012
- [41] A. Coelho, TOPAS and TOPAS-Academic: an optimization program integrating computer algebra and crystallographic objects written in C++, J. Appl. Crystallogr., 51 (2018) 210-218 https://doi.org/10.1107/S1600576718000183
- [42] B. Ravel, M. Newville, ATHENA, ARTEMIS, HEPHAESTUS: data analysis for X-ray absorption spectroscopy using IFEFFIT, Journal of Synchrotron Radiation, 12 (2005) 537-541 https://doi.org/doi:10.1107/S0909049505012719
- [43] K. Momma, F. Izumi, VESTA 3 for three-dimensional visualization of crystal, volumetric and morphology data, J. Appl. Crystallogr., 44 (2011) 1272-1276 https://doi.org/10.1107/S0021889811038970
- [44] V. Pamidi, S. Trivedi, S. Behara, M. Fichtner, M.A. Reddy, Micron-sized single-crystal cathodes for sodium-ion batteries, iScience, 25 (2022) 104205 https://doi.org/10.1016/j.isci.2022.104205
- [45] Z. Zhang, R. Wang, J. Zeng, K. Shi, C. Zhu, X. Yan, Size Effects in Sodium Ion Batteries, Adv. Funct. Mater., 31 (2021) 2106047 https://doi.org/10.1002/adfm.202106047
 [46] J.F. Moulder, J. Chastain, Handbook of X-ray Photoelectron Spectroscopy: A Reference Book of Standard Spectra for Identification and Interpretation of XPS Data, Physical Electronics Division, Perkin-Elmer Corporation1992.

- [47] S. Hüfner, Photoelectron spectroscopy: principles and applications, Springer Science & Business Media2013.
- [48] L. Wang, Y.-G. Sun, L.-L. Hu, J.-Y. Piao, J. Guo, A. Manthiram, J. Ma, A.-M. Cao, Copper-substituted Na_{0.67}Ni_{0.3-x}Cu_xMn_{0.7}O₂ cathode materials for sodium-ion batteries with suppressed P2–O2 phase transition, J. Mater. Chem. A, 5 (2017) 8752-8761 https://doi.org/10.1039/C7TA00880E
- [49] M.H. Han, E. Gonzalo, N. Sharma, J.M. López del Amo, M. Armand, M. Avdeev, J.J. Saiz Garitaonandia, T. Rojo, High-Performance P2-Phase Na_{2/3}Mn_{0.8}Fe_{0.1}Ti_{0.1}O₂ Cathode Material for Ambient-Temperature Sodium-Ion Batteries, Chem. Mater., 28 (2016) 106-116 https://doi.org/10.1021/acs.chemmater.5b03276
- [50] Q. Huang, Y. Feng, L. Wang, S. Qi, P. He, X. Ji, C. Liang, S. Chen, L. Zhou, W. Wei, Structure modulation strategy for suppressing high voltage P3-O1 phase transition of O3-NaMn_{0.5}Ni_{0.5}O₂ layered cathode, Chem. Eng. J., 431 (2022) https://doi.org/10.1016/j.cej.2021.133454
- [51] J. Chen, L. Li, L. Wu, Q. Yao, H. Yang, Z. Liu, L. Xia, Z. Chen, J. Duan, S. Zhong, Enhanced cycle stability of Na_{0.9}Ni_{0.45}Mn_{0.55}O₂ through tailoring O3/P2 hybrid structures for sodium-ion batteries, J. Power Sources, 406 (2018) 110-117 https://doi.org/10.1016/j.jpowsour.2018.10.058
- [52] Y. Liu, D. Wang, P. Li, Y. Liu, Y. Sun, Y. Liu, B. Zhong, Z. Wu, X. Guo, The Relationship between Initial Coulombic Efficiency and Transition Metal Ion Redox in P2-Na_{0.85}[Cu_{0.1}Fe_xMn_{1-x}]O₂ Cathodes, Industrial & Engineering Chemistry Research, 61 (2022) 11494-11503 https://doi.org/10.1021/acs.iecr.2c01864
- [53] H.N. Vasavan, M. Badole, S. Dwivedi, S. Kumar, Structural and transport properties of P2-Type Na_{0.70}Ni_{0.20}Cu_{0.15}Mn_{0.65}O₂ layered oxide, Ceram. Int., 48 (2022) 28986-28993 https://doi.org/10.1016/j.ceramint.2022.04.206

[Supplementary Information]

Unveiling the Potential of P3 Phase in Enhancing the

Electrochemical Performance of a Layered Oxide

Cathode

Hari Narayanan Vasavan ^a, Manish Badole ^a, Samriddhi Saxena ^a, Velaga Srihari ^b, Asish Kumar Das ^a, Pratiksha Gami ^a, Sonia Deswal ^c, Pradeep Kumar ^c, and Sunil Kumar ^{a,*}

^a Department of Metallurgical Engineering and Materials Science, Indian Institute of Technology Indore, Simrol, 453552, India.

^b High Pressure & Synchrotron Radiation Physics Division, Bhabha Atomic Research Centre, 400085 Mumbai, India

^c School of Physical Sciences, Indian Institute of Technology Mandi, Himachal Pradesh, 175005, India

* Corresponding Author, sunil@iiti.ac.in

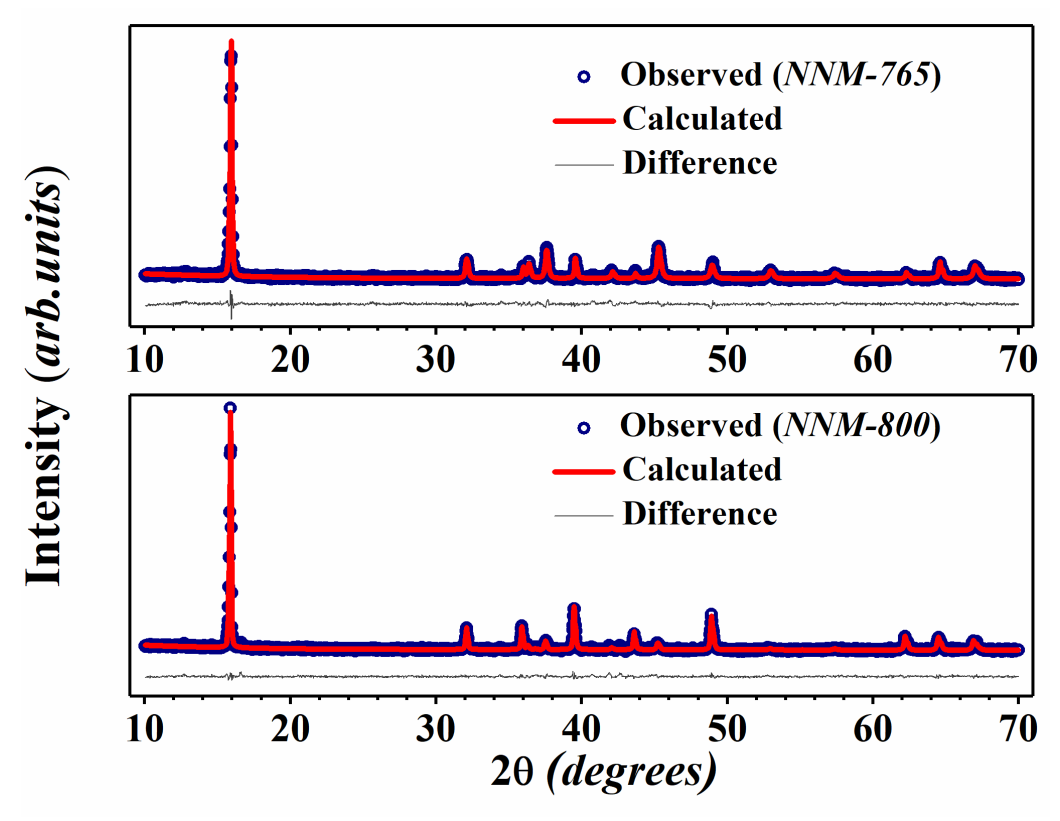


Fig. S1: Rietveld refinement profiles of XRD data of NNM-765 and 800 samples.

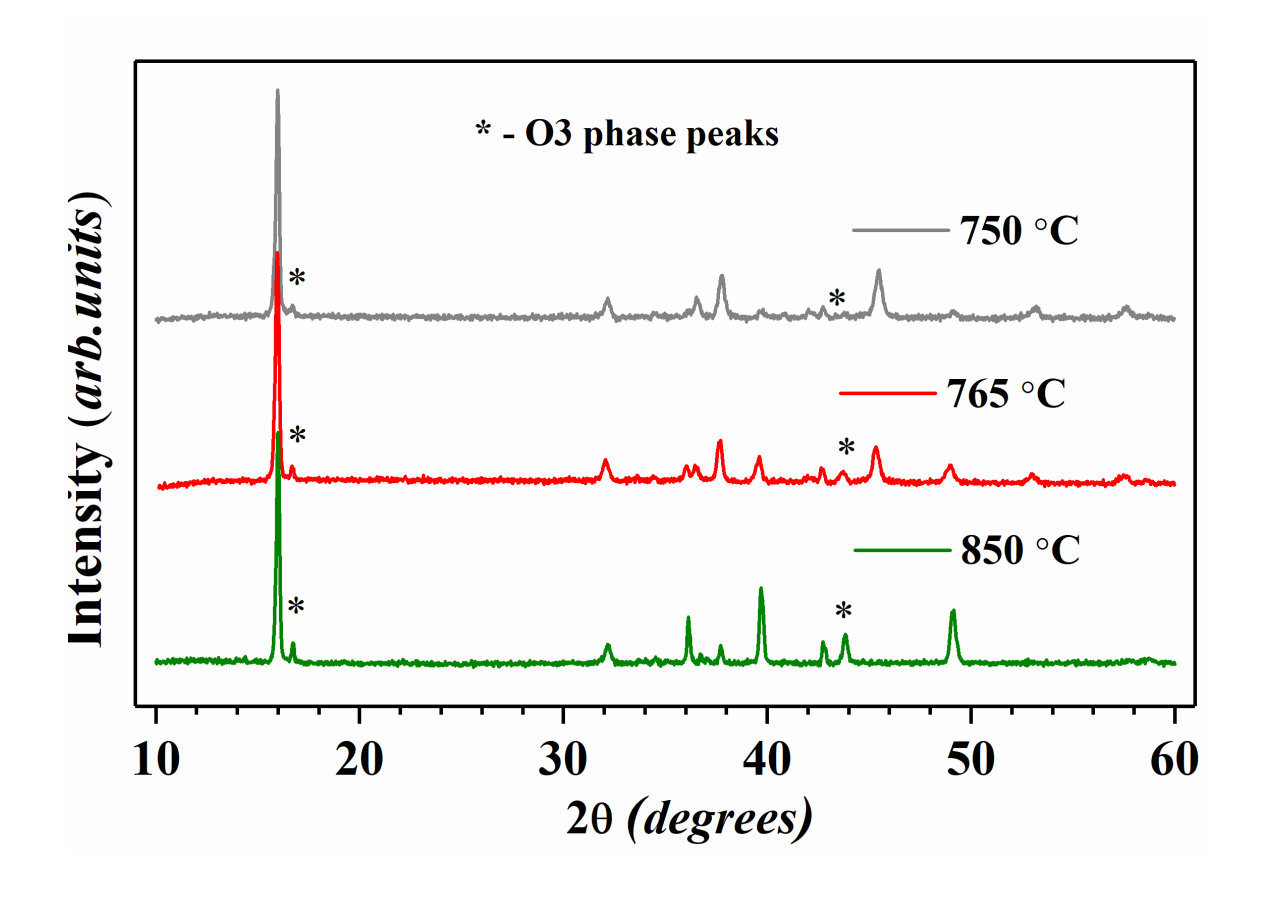


Fig. S2: Room temperature XRD patterns of NNM-750, 765, and 850 synthesized with 5% extra Na₂CO₃.

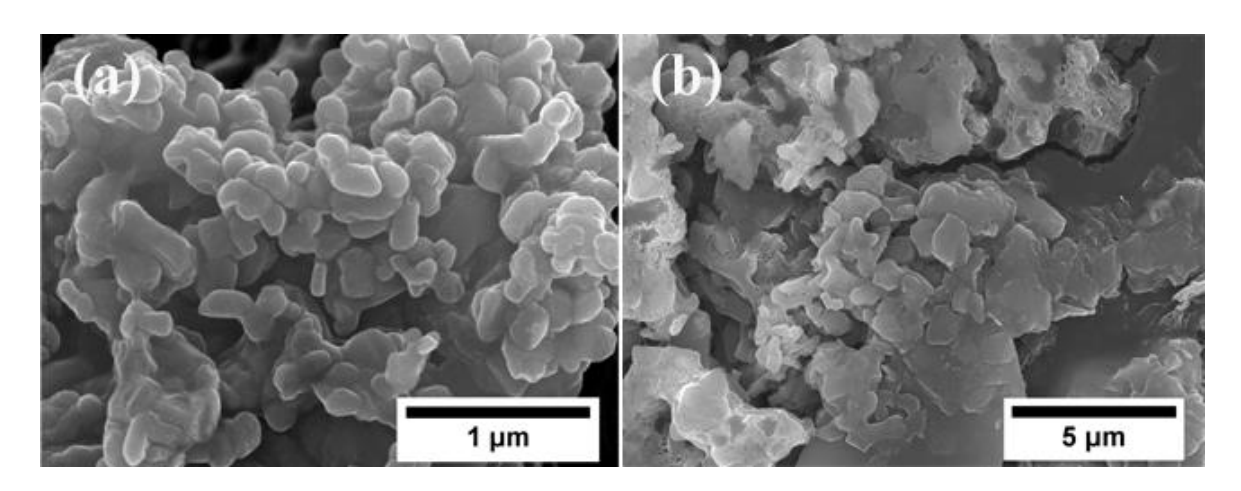


Fig. S3: SEM images of (a) NNM-765 and (b) NNM-800.

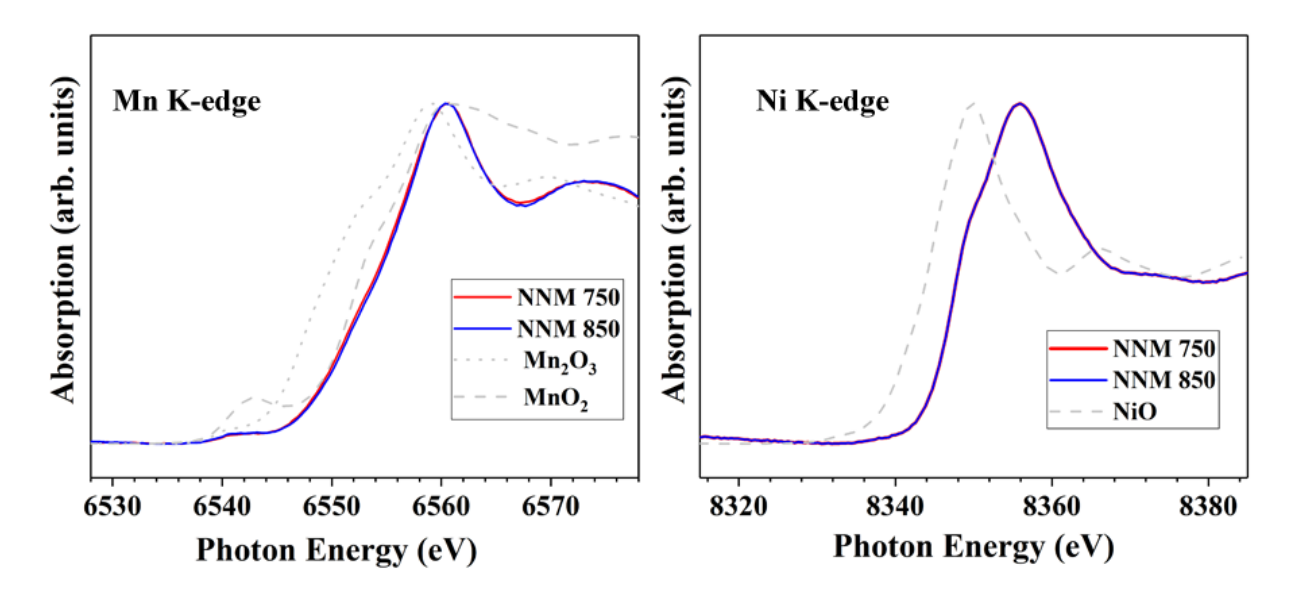


Fig. S4: Normalized XANES spectra of NNM-750 and 850 at Mn and Ni K edges along with related reference compounds.

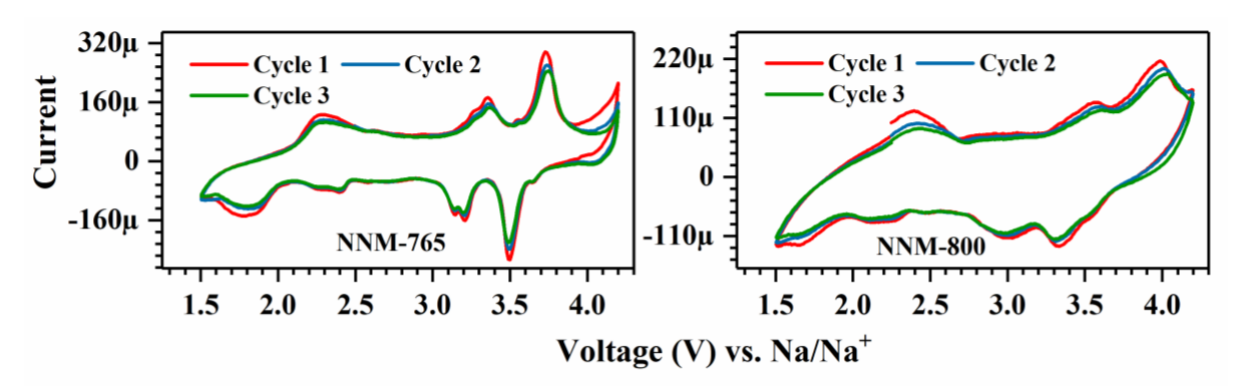


Fig. S5: Cyclic voltammograms of NNM-765 and 800.

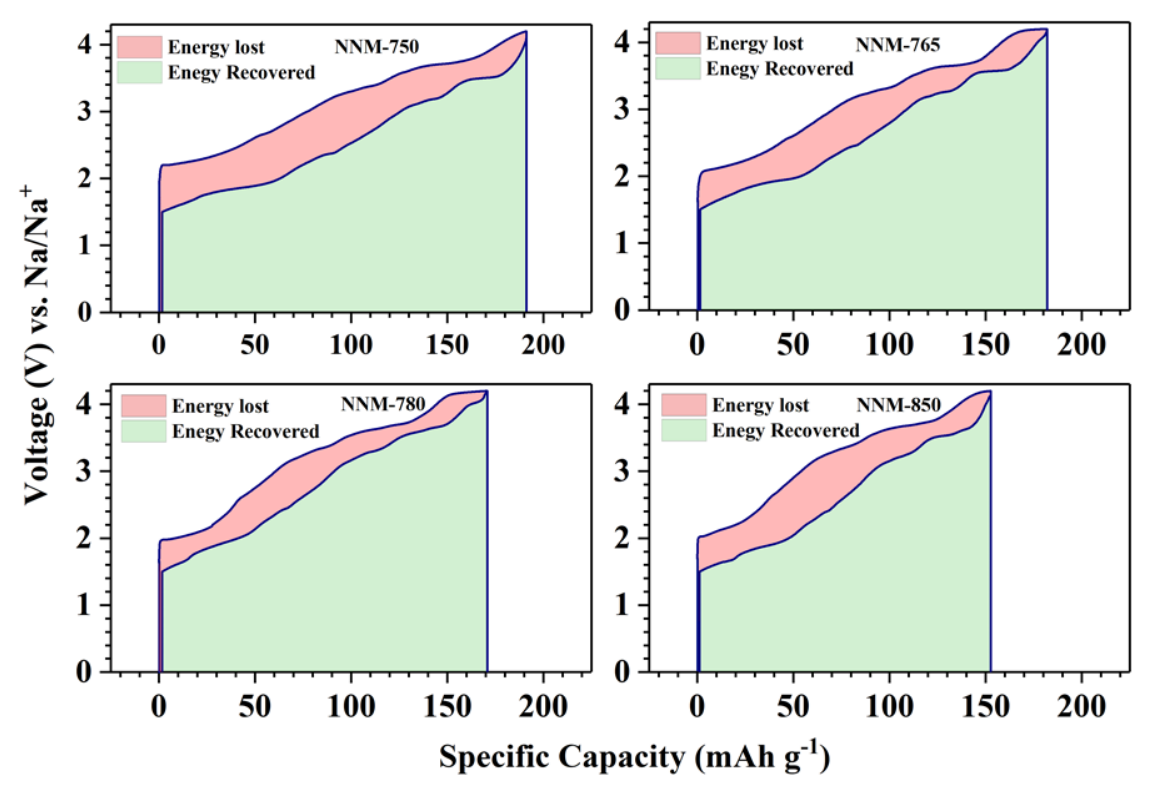


Fig. S6: GCD curves of NNM-750, 765, 780, and 850 depicting energy loss and energy recovered during discharge.

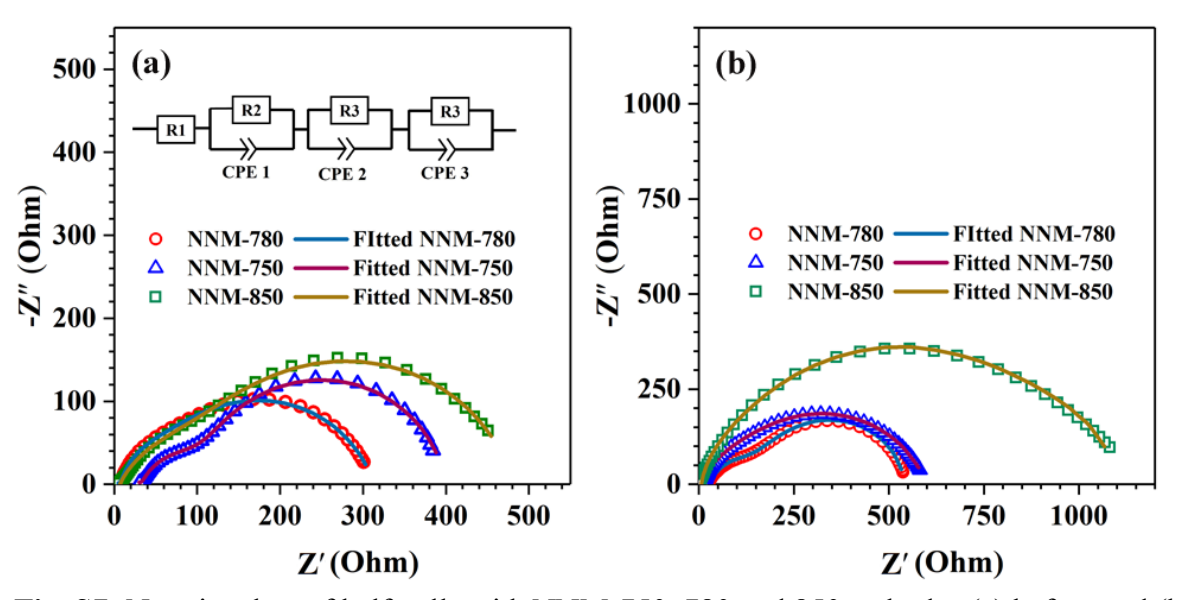


Fig. S7: Nyquist plots of half-cells with NNM-750, 780 and 850 cathodes (a) before and (b) after cycling. The impedance data in Fig. S7 was fitted using the equivalent circuit shown in the figure insets.

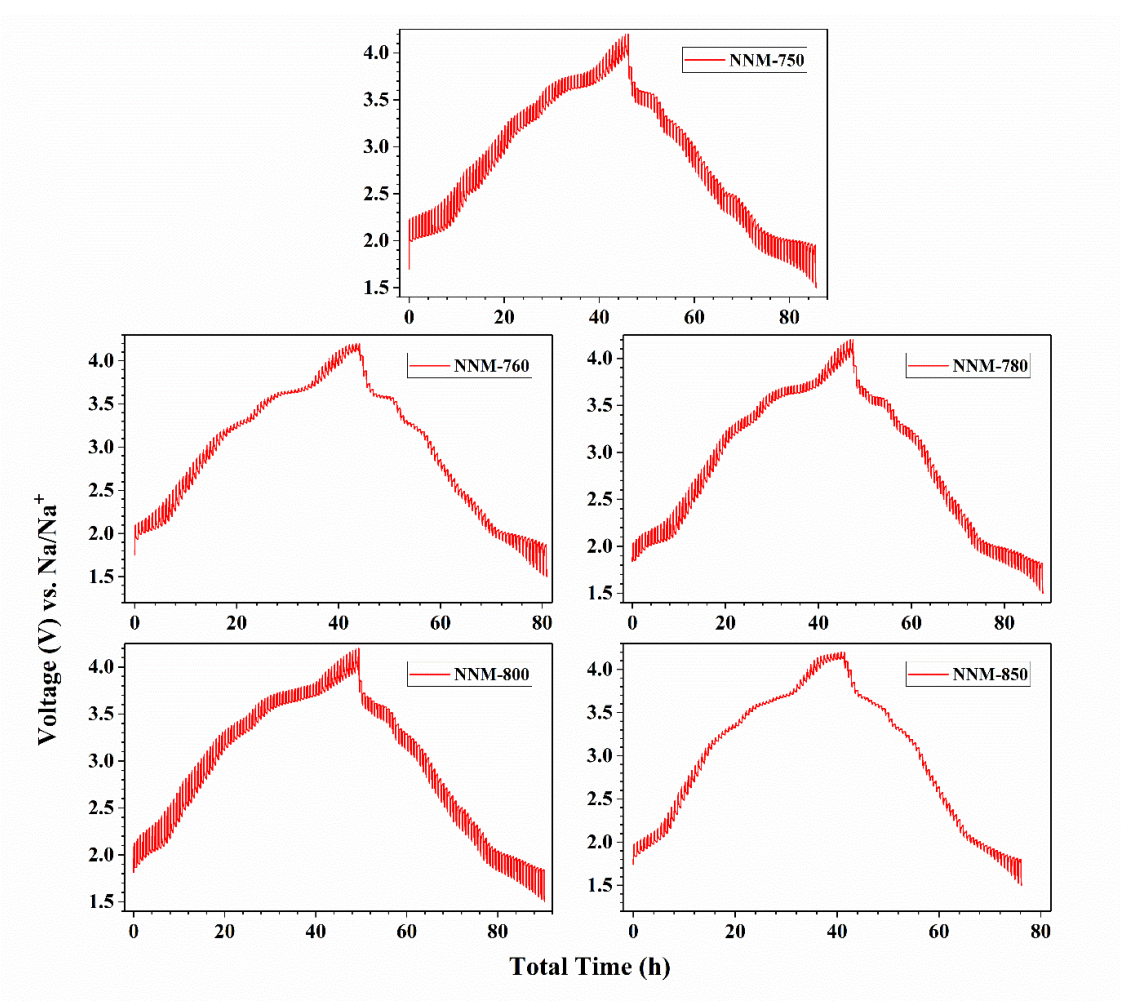


Fig. S8: GITT curves of NNM-*x* series of cathodes.

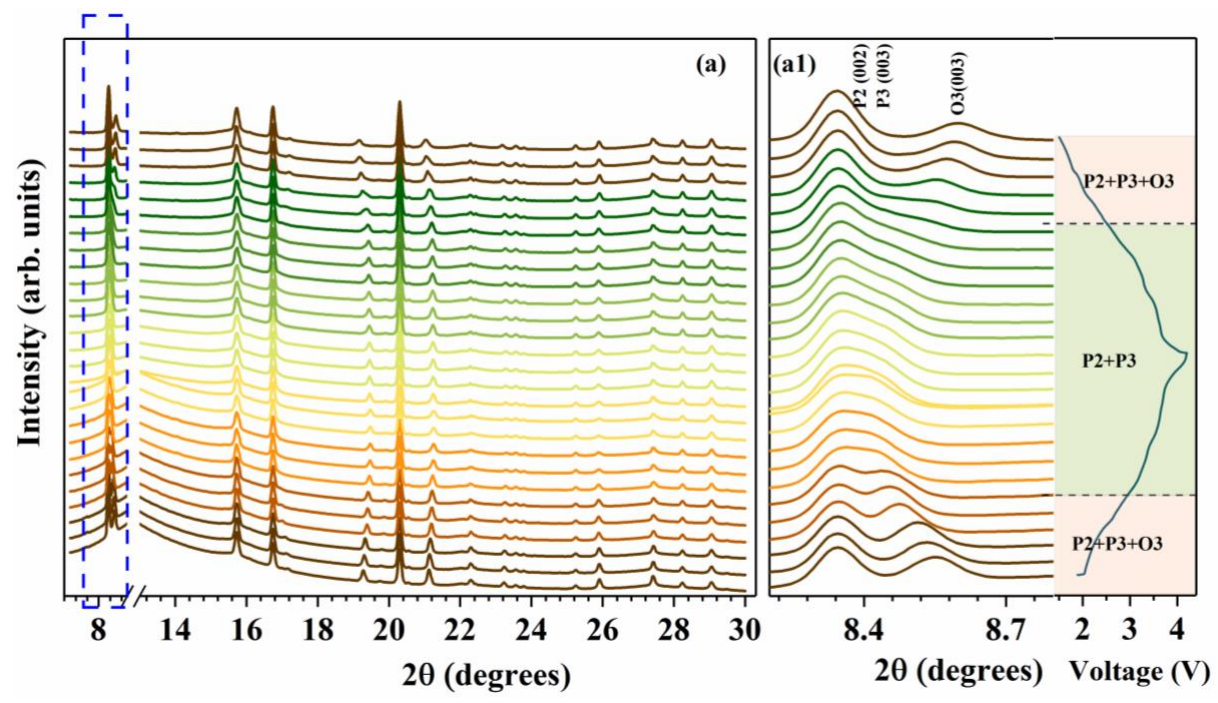


Fig. S9: (a) Operando SXRD patterns of NNM-780 with (a1) depicting the zoomed portion between a 2θ range of 8° to 9° .